

# An Evolutionary Shaking-Forecast-Based Earthquake Early Warning Method

Aldo Zollo<sup>1</sup>, Simona Colombelli<sup>1</sup>, Alessandro Caruso<sup>2</sup>, and Luca Elia<sup>1</sup>

<sup>1</sup>University of Naples Federico II

<sup>2</sup>University of naples Federico II

April 3, 2023

1

2

3

## **An Evolutionary Shaking-Forecast-Based Earthquake Early Warning Method**

4

5 Aldo Zollo, Simona Colombelli, Alessandro Caruso\* and Luca Elia

6 Department of Physics, University of Naples Federico II

7 \*now at RFI, Rete Ferroviaria Italiana, Rome

8 **Abstract**

9

10 Here we propose a methodology for Earthquake Early Warning able to issue the alert based on the  
11 real-time estimation of the epicentral area where a peak ground Intensity measure is expected to  
12 exceed a user-set ground shaking level. The method provides in output a P-wave-based, time-  
13 evolutive “early” shake map. It combines the Peak Ground Velocity (PGV) predictions available  
14 from the observed P-wave amplitudes and from the region-specific Ground Motion Prediction  
15 Equation (GMPE), using progressively updated estimates of earthquake location and magnitude.  
16 The P-wave displacement, velocity and acceleration amplitudes are jointly measured on a  
17 progressively expanded P-wave time window while the earthquake location and magnitude are  
18 evaluated using the first P-arrival time and displacement amplitudes at near source stations. A  
19 retrospective analysis of the 2016, Mw 6.5 Central Italy earthquake records shows that depending  
20 on the network density and spatial source coverage, the method naturally accounts for effects  
21 related to the earthquake rupture directivity and spatial variability of strong ground motion related  
22 to crustal wave propagation and site amplification. Within 1.5 sec since the first alert (5.15 sec  
23 after the origin time), the simulated performance of the system in predicting the event ground

---

\* Now at RFI, Rete Ferroviaria Italiana, Rome

24 shaking is very high: in the 40 km-radius area that suffered an Intensity MCS VIII-IX, 41 over 42  
25 strong-motion instrumented sites would have been successfully alerted, with only one false alarm.  
26 Even considering the calculated blind-zone of 15 km radius, a 15-55 km wide annular area would  
27 have received the alert 2-14.5 sec before the occurrence of the strong ground shaking.  
28 The proposed EEW method evolves with time in a way that it minimizes the missed alarms while  
29 increasing successful alarms and to a lesser extent false alarms, so it is necessary for the end-user  
30 to accept these possibilities and account for them in a probabilistic decision scheme depending on  
31 the specific safety actuation measure to be undertaken in real-time.

32

### 33 **1. INTRODUCTION**

34 Earthquake Early Warning (EEW) systems are modern, real-time seismic monitoring infrastructures  
35 aimed at issuing an alert and activating emergency safety measures to protect people, buildings,  
36 and industrial facilities in advance to the impact of strong and potentially damaging shaking waves.  
37 The basic principle on which network-based EEW systems ground on, is to use the time lag  
38 between the alert message issuance and the arrival of damaging seismic waves, to broadcast an  
39 alert soon after the first P-waves are detected at a near-source deployed, seismic network. The  
40 early warning can reach seconds or tens of seconds in advance the sites to be protected against  
41 the arrival of strong shaking waves, depending on the travel distance from the source.  
42 Onsite or stand-alone early warning systems use a single station or small-aperture arrays of  
43 sensors deployed in proximity of the target site to secure. In this case, the measures of the initial P-  
44 wave amplitude and/or the dominant signal frequency can be used as proxies for the late arriving,  
45 strongest shaking wave amplitudes at the same site, with no need for information on the  
46 earthquake location and magnitude (*Wu and Kanamori [2005]*). Along this same research direction  
47 we mention , among others, the algorithm that has been developed to estimate the seismic  
48 intensity from real-time early P-wave signals (*Yamamoto et al., 2008*), the threshold-based method

49 that uses the time-domain measurement of the cumulative absolute velocity from strong motion  
50 records (Alcik et al.,2009) and the B-delta method that estimates the earthquake epicentral  
51 distance and magnitude from modelling the rise of the early P-wave amplitude envelope (Odaka et  
52 al., 2003).

53 In the cases where a network of stations is deployed in the source area, network-based EEW  
54 systems analyze the early P-wave signals recorded at the stations, detect the occurrence of the  
55 earthquake, determine its location and magnitude and estimate its shaking potential to nearby and  
56 distant sites, using previously calibrated empirical attenuation relationships (Ground Motion  
57 Prediction Equations, GMPE). The alert notification can reach any distant site within a time interval  
58 from the earthquake origin that typically ranges from a few seconds (few tens of kilometers from  
59 the source) to several tens of seconds (a hundred kilometers from the source). Different factors  
60 may influence the “lead-time”, i.e., the delay between the arrival of the strongest shaking waves at  
61 the target site and the first alert time. Among them, the distance between the source area and the  
62 target site, the geometry of the network, the time of event detection, the time needed for the  
63 automatic waveform analysis and telemetry and, lastly, the complexity of the source.

64 During the last two decades EEW systems have been widely developed and experimented in  
65 several high seismic hazard countries around the world, such as Japan, USA, Mexico, Taiwan, and  
66 China (*Allen and Melgar [2019]*). In Europe, several active seismic countries, mostly along the  
67 Mediterranean region (Italy, Romania, Switzerland, Turkey, Greece, and the Ibero-Maghrebian  
68 region), are nowadays experimenting and testing the use of EEW systems mainly for research  
69 purposes, while the technological components of the operational seismic monitoring systems are  
70 yet not fully real-time compliant, such that they can be an effective tool for fast seismic risk  
71 mitigation actions (*Clinton et al. [2016]*).

72 Most of the existing EEW systems are based on the standard concepts either of the network-based  
73 system or of the on-site approach. In some cases, such as in Japan, where the station density and

74 coverage are high and uniform all over the country and where the largest magnitude earthquakes  
75 may occur offshore, the nation-wide EEW systems benefit from the early P-wave detection at  
76 coastline stations (in an on-site approach), for issuing the warning at inland sites. However, the  
77 actual integration of the onsite and network-based approaches is under development in Japan,  
78 USA and China for providing the output for a timely and robust alert decision scheme.

79 The Japan Meteorological Agency (JMA) is currently testing the propagation of local undamped  
80 motion (PLUM) method (*Kodera et al. [2018]*), a wavefield-based EEW approach that predicts  
81 seismic intensities directly from spatial inter- and extra-polation of the observed real-time ground  
82 motion measures near target sites. When integrated with standard point-source EEW methods, the  
83 PLUM method showed an improved performance in terms of more accurate ground-motion  
84 prediction for large earthquake rupture and event detection and declaration in case of multiple  
85 events sequences.

86 Whichever configuration is used, the standard approaches to EEW are based on simplified  
87 assumptions and models both for the earthquake source and wave propagation processes. This  
88 may result in highly uncertain predictions of the earthquake peak shaking and therefore in an  
89 unacceptable large number of missed or false alarms (*Minson et al. [2019]*).

90 To account for the earthquake source finiteness, different methodologies have been recently  
91 proposed and developed to estimate in real-time the fault geometry and size from early P and S-  
92 wave signals collected at near-source stations.

93 The FinDer (Finite Fault Rupture Detector) algorithm (*Böse et al. [2012]*), assumes a line source and  
94 can automatically detect in real-time its surface projection, the current centroid position, length,  
95 and strike, by comparing the real-time ground motion amplitudes to a set of pre-calculated  
96 templates, using image recognition techniques. Errors in length estimates are typically on the same  
97 order as station spacing in the network so that the method turns out to be useful for accurate  
98 earthquake early warnings wherever the station density is sufficiently high.

99 Real-time inversion of amplitudes recorded by high-frequency GPS stations have also been  
100 explored to improve the finite fault description in terms of magnitude and source length (*Allen and*  
101 *Ziv [2011]; Colombelli et al. [2013]; Grapenthin et al. [2014]*). In these approaches, the permanent  
102 static offset produced by large earthquakes (i.e., the coseismic ground deformation) is inverted in  
103 real-time to infer the slip distribution on the fault plane, assuming a prior determined fault  
104 orientation. The real-time magnitude and the along-strike extent of the rupture area are finally  
105 used to predict the expected ground shaking due to the finite source.

106 More recently, the progressive measurement of the P wave displacement amplitude has been  
107 proposed to obtain a fast characterization of the extended earthquake source, in terms of  
108 magnitude and expected length of the rupture (*Colombelli and Zollo [2015]; Nazeri et al. [2019];*  
109 *Zollo et al. [2021a]*). In this approach, the Logarithm of P-wave amplitude vs Time (LPDT curve) is  
110 used as a proxy for the Moment Rate Function, allowing for the real-time tracking of the source  
111 process evolution and for a rapid characterization of seismic moment and source rupture duration,  
112 in the hypothesis of a triangular shape for describing the source process.

113 Here we present a new methodology that integrates the network and on-site approaches for the  
114 alert release. The methodology is based on the real-time, evolutionary mapping of the Potential  
115 Damage (or strong shaking) Zone (PDZ) as represented by a predicted Intensity Measure (IM), such  
116 as the peak ground velocity/acceleration or the instrumental intensity. The methodology  
117 incorporates the more recent techniques for a refined estimation of the main source parameters  
118 (earthquake location and magnitude) and P-wave-based, peak motion forecast (e.g., *Colombelli*  
119 *and Zollo, 2015; Caruso et al., 2017 and Zollo et al., 2021*) that are used to predict the expected  
120 ground shaking level at sites not instrumented by strong motion sensors.

121 Previous studies, in several seismic regions worldwide, have shown that the P-peak initial  
122 amplitude is a natural proxy for the late maximum amplitude of seismic records acquired from  
123 near-source to regional distance range (epicentral distance < 100 km) (*Wu and Kanamori [2005];*

124 Zollo et al. [2010]). An empirical log-log relationship is usually adopted to correlate the Peak  
125 ground motion on the entire signal (in acceleration - PGA - or velocity - PGV) to the initial P-wave  
126 peak amplitude ( $P_a$ ,  $P_v$  or  $P_d$ ), measured in a short time window (1 to 5 s) after the P-wave arrival.  
127 These empirical relations have been proposed and used in onsite EEW applications to predict the  
128 peak ground shaking of the potential damaging event, by-passing the estimation of source  
129 magnitude and location.

130 In the proposed method, previous calibrated empirical relations between early P-wave amplitudes  
131 and peak ground motion parameters are used to predict the shaking intensities at instrumented,  
132 recording sites. As the P wavefront propagates across the network, a time-varying, *early* shake map  
133 is built through a physics-based interpolation approach, which combines the available observed, P-  
134 wave and GMPE predicted PGV (following Worden et al. [2010]).

135 Here we evaluate the performance of the proposed methodology through its offline application to  
136 the October 30, 2016,  $M_w$ 6.5 Norcia (Central Italy) earthquake records and discuss the system  
137 performance in forecasting the earthquake peak ground shaking.

138

## 139 **2. METHOD**

140 The methodology combines specific modules aimed at sequential operations, going from  
141 earthquake detection and location to magnitude determination and peak ground shaking  
142 prediction. The block diagram of the method is shown in Figure 1, while the detailed theory and  
143 implementation of the main steps are described separately in the following sections. The adopted  
144 strategy is to combine the principles of onsite EEW methods (Peak ground shaking prediction by P-  
145 wave amplitude measurements) and those of network-based approaches (real-time location,  
146 magnitude estimation and PGV prediction through regional-specific GMPEs).

147

### 148 **2.1 Earthquake detection and location**

149 The system is designed to process the 3-component, ground acceleration records, as acquired by a  
150 real-time, dense network deployed in the earthquake epicentral area and extending to local and  
151 regional (100 km) distances. The first P-wave arrival time signals are detected by the real-time  
152 Filter-Picker 5 algorithm (*Lomax et al. [2012]*) on the vertical component of the acceleration  
153 waveforms.

154 As soon as the first two stations have triggered the event, a real-time location estimate is obtained  
155 by using a real-time version of the M-PLOC algorithm described in *Zollo et al. [2021b]*. M-PLOC  
156 provides a probabilistic solution for the earthquake location, based on the real-time measure of  
157 three different observed quantities (differential arrival times, amplitude ratios, and back-azimuth  
158 from the P-wave polarization) evaluated in progressive (or fixed) time windows after the first P-  
159 wave arrival. The most probable estimates of hypocenter coordinates and origin time are provided  
160 as soon as the first stations trigger the event and are progressively updated as the P-wave front  
161 expands across the network and new portions of signals are acquired by more and more distant  
162 stations. In the present application only the differential arrival times at pairs of stations within the  
163 network have been used for earthquake location, since preliminary tests confirmed that the  
164 azimuthal coverage of stations was sufficiently dense to get optimal location without using  
165 additional parameters.

166 When using only differential P-arrival times, the M-PLOC method determines the earthquake  
167 location as the maximum likelihood location contained in a gridded 3-D crustal volume. A  
168 minimum of 2 stations where the first P-arrival is detected are used to get the first earthquake  
169 location. In this case the epicenter location is set at the half-length of the surface segment joining  
170 the two station locations and a trial-depth value is assumed. In the the case-study application  
171 considered in this paper a trial-depth of 10 km has been set based on the historical seismicity of  
172 the area, but this initial value can be adjusted according to the characteristic depth distribution of  
173 historical seismicity in other seismic regions of interest. However, after few iterations this initial

174 location is updated as more P-wave arrival time data are available. With three or more stations at  
175 which the P-arrival is detected, the mutual differential times allow to constrain the hypocenter  
176 location with an accuracy that is progressively improved as more P-arrival times are available from  
177 the automatic picking. Details about the earthquake location uncertainty estimates inferred from  
178 the PDF distribution can be found in Zollo et al. [2021b].

179

## 180 2.2 Peak parameter measurement

181 Following the onsite method and starting from the P-wave arrival time, we measure the initial  
182 peak amplitude parameters,  $P_a$ ,  $P_v$  and  $P_d$ , as the absolute, maximum value of the vertical  
183 component of acceleration, velocity and displacement, respectively. The measures are repeated  
184 every 0.5 sec and are stopped at the expected arrival of the S-waves, as predicted by the  
185 earthquake location. The acceleration records are first processed by removing the mean value and  
186 the linear trend. Waveforms are then integrated once to obtain velocity waveforms and the linear  
187 trend is removed again, prior to measure  $P_v$ . A second integration is performed to get  
188 displacement traces, followed by a causal, high-pass Butterworth filter, to remove the artificial low-  
189 frequency drifts and baselines on displacement traces, which may appear from the double  
190 integration operation (Boore et al. [2002]). Following the approach already used by Caruso et al.  
191 [2017], we automatically select the proper cut-off frequency for the filter, which can be either  
192 0.075Hz or 1Hz, depending on the quality of the input data, as briefly recalled in the following  
193 lines. Two parameters are used to evaluate the quality of data: the signal-to-noise ratio ( $SNR$ ) and  
194 the  $P_d/P_v$  ratio. Specifically, the  $SNR$  is computed as  $SNR = 20 * \log_{10}(P_d/P_d^N)$ , where  $P_d$  is  
195 measured on the available signal in the selected time window and  $P_d^N$  is the maximum  
196 displacement of the pre-event noise, over the same time window. As for the  $P_d/P_v$  ratio, both  
197 peak amplitude parameters are measured in the same time window. Based on the idea that  $P_d$  and  
198  $P_v$  follow a linear, constant-coefficient empirical relation with magnitude and logarithm of

199 hypocentral distance, their ratio is therefore expected to vary in a predetermined range around a  
200 constant level. On the contrary, out-of-range  $P_d/P_v$  values indicate noisy data, with the peak  
201 displacement possibly contaminated by artificial long-period distortions. The observed values of  
202  $SNR$  and of the  $P_d/P_v$  ratio are therefore compared to predetermined threshold values, for the  
203 automatic selection of the proper filter, or data are eventually discarded if the quality control is  
204 failed (see *Caruso et al.* [2017], for further details).

205

### 206 2.3 Magnitude estimation

207 As in network-based approaches, in our method the real-time moment magnitude ( $M_w$ ) is  
208 obtained by averaging the single magnitude estimates derived from the three P-peak amplitude  
209 parameters ( $P_a, P_v$  and  $P_d$ ), measured at few near-source stations. Given a recording station at  
210 hypocentral distance  $R$ , for each parameter, we use an empirical attenuation relationship to  
211 estimate the moment magnitude, of the form (*Wu et al.* [2006]; *Zollo et al.* [2006]):

$$M_w^x = A_x \cdot \log P_x + B_x \cdot \log R + C_x \quad \#(1)$$

212 where  $x = a, v, d$  indicates acceleration, velocity and displacement P-waveform records. The  
213 method requires that the coefficients of eq.(1) should be previously derived from the  
214 retrospective, empirical regression analysis of different magnitude-distance earthquake records in  
215 the seismic region of concern. In this study, for demonstration purposes, the coefficients  $A_x, B_x$   
216 and  $C_x$  are determined by a linear regression analysis using an existing earthquake data set in  
217 Central Italy, the region of our earthquake-application case study (see section 3)

218 For a given station  $i$  and for each time step  $t$ , the magnitude value is obtained by the weighted  
219 average of all the available predictions:

$$M_w^{it} = \frac{w_a \cdot M_w^a + w_v \cdot M_w^v + w_d \cdot M_w^d}{w_a + w_v + w_d} \quad \#(2)$$

220 where the weights  $w_x$  are estimated from the standard errors  $\sigma'_x$  of empirical relations (1) as

221  $w_x = \frac{1}{\sigma_x^2}$ . Finally, considering that at the time step  $t$ , a total of  $N$  stations has recorded the P-wave  
222 signal with a variable signal length  $T_d^{it}$  ( $i$  is the station index), the final, average magnitude is  
223 obtained as:

$$M_w^t = \frac{1}{\sum_1^N T_d^{it}} \sum_{i=1}^N T_d^{it} \cdot M_w^{it} \quad \#(3)$$

224 where the signal length  $T_d^{it}$  is used to weigh the station-magnitude values. Here we assume that  
225 the estimates inferred from larger portion of P-wave signals must have a larger weight than those  
226 obtained from shorter time windows. In our approach, the magnitude is computed using only  
227 stations that satisfy a specific criterion, as explained below.

228 A previous study (e.g., *Colombelli et al.* [2015]) has shown that the joint use of the three P-peak  
229 amplitude parameters allows improving the accuracy and reducing the uncertainty on magnitude  
230 estimation, especially when a limited time window and number of stations are available for the  
231 measurement. Furthermore, initial P-wave observation of real earthquakes have shown that when  
232 expanding the time window, the three peak amplitude parameters generally increase with time.  
233 The typical Logarithm of P-peak Displacement vs Time (LPDT) curve starts from small values and  
234 reaches a stable plateau level at a corner-time that depends on the final event magnitude  
235 (*Colombelli et al.* [2012; 2014]; *Trugman et al.* [2019]). Additionally, *Colombelli and Zollo* [2015]  
236 observed the dependency on magnitude of this corner-time and used it to estimate the fault  
237 length of earthquakes in Japan. *Nazeri et al.* [2019] and *Trugman et al.* [2019] confirmed this  
238 general behavior of LPDT curves by analyzing extended datasets for Japanese and Central Italy  
239 earthquake sequences. More recently, *Zollo et al.* [2021a] propose a technique to determine the  
240 rupture radius of a circular earthquake rupture from the estimations of the corner-time of  
241 azimuthally averaged LPDT curves.

242 Given the general increasing amplitude of initial P-wave peak parameters with time, reliable  
243 magnitude estimates can be obtained only for  $P_x$  values measured at the plateau of the curves,

244 while significant magnitude underestimations can generally occur using shorter time windows (i.e.,  
245 while the curve is still increasing). In our method, to avoid the initial underestimations, we  
246 developed an automatic algorithm able to identify the plateau time of the curves, by continuously  
247 monitoring their time derivative and evaluating when it reaches a near-to-zero threshold value. At  
248 this time, i.e., when the plateau has been reached, the corresponding peak parameters start being  
249 used for the magnitude determination. It is worth to note that the three curves (LPAT, LPVT, and  
250 LPDT) are expected to reach the plateau level nearly at the same time (*Colombelli et al.* [2014];  
251 *Nazeri et al.* [2019]), thus, for computational simplicity, we only monitor the time derivative of the  
252 LPVT curve. Figure 2 shows some examples of recorded seismograms (in acceleration) at a few  
253 stations around the epicenter and the corresponding computation of LPDT curves, which are  
254 available at sequential times, as the P-wave front propagates across the array. Finally, to ensure a  
255 rapid convergence to the final magnitude of the event, only the recordings within 100km from the  
256 epicenter are used for the magnitude computation, or alternatively a maximum of 30 triggered  
257 stations.

258

#### 259 2.4 Computation of the “Early” Shake-Map

260 With the aim of building real-time reliable, P-wave based, shake maps, we predict the peak ground  
261 motion in the region of interest using two different approaches, one for the recording sites and  
262 another for the *virtual* nodes, i.e., the not-instrumented grid nodes. Specifically, the Peak Ground  
263 Velocity (PGV) at the recording sites is predicted from the recorded P-amplitudes of the early P-  
264 wave signals using eq. 1 (onsite approach). The PGV at the *virtual* nodes is instead predicted  
265 through a physics-based interpolation techniques which uses the available regional ground motion  
266 prediction equation (GMPE) and real-time estimates of earthquake location and magnitude  
267 (network-based approach). The two approaches are described in detail in the following sections.

##### 268 2.4.1 Peak ground motion prediction at the recording sites

269 Like what has been done for the magnitude, the three peak amplitude parameters  $P_a$ ,  $P_v$  and  $P_d$   
270 measured at the recording sites for each time window  $t$ , are jointly used to predict the expected  
271 PGV, based on a scaling relationship of the form:

$$272 \quad \log PGV_x^t = D_x \cdot \log P_x^t + E_x; \quad w_x = \frac{1}{\sigma_x^2} \quad (4)$$

273 Where  $D_x, E_x$  are the empirically estimated coefficients and  $\sigma_x$  are the standard errors of the  
274 relationship between the PGV and the  $P_x$  parameter. Coefficients D and E are empirically  
275 estimated using a linear regression analysis, for each peak amplitude parameter ( $P_x$ ) and each time  
276 window ( $t$ ). An example of data and linear regression for the 3-s time window is shown in Figure S3  
277 of the Supplemental Material, while the full list of estimated coefficients (and their uncertainties)  
278 is reported in Table S2 of the Supplemental Material. The predicted value of  $\log PGV$  and its  
279 uncertainty at any time  $t$  are therefore obtained as the weighted average of the three estimated  
280  $\log PGV_x^t$  values:

$$\log PGV_{onsite}^t = \frac{w_a \cdot \log PGV_a^t + w_v \cdot \log PGV_v^t + w_d \cdot \log PGV_d^t}{w_a + w_v + w_d} \quad \#(5)$$

281

$$\sigma_{\log PGV_{onsite}} = \sqrt{\frac{w_a \cdot \left(\log \frac{PGV_a^t}{PGV_{onsite}^t}\right)^2 + w_v \cdot \left(\log \frac{PGV_v^t}{PGV_{onsite}^t}\right)^2 + w_d \cdot \left(\log \frac{PGV_d^t}{PGV_{onsite}^t}\right)^2}{w_a + w_v + w_d}} \quad \#(6)$$

282

283 Coefficients D and E of equation (4) are region-specific and must be preliminary determined  
284 through analyses that use data from past earthquakes recorded in the region of interest.  
285 Furthermore, the algorithm is designed to monitor both the vertical and the horizontal  
286 components. The predicted PGV from the vertical  $P_x$  amplitude is continuously compared to the  
287 PGV value measured on the horizontal components. At any time along the waveform, the  
288 maximum between these two values is used as the peak ground motion estimate.

289 At the end of the event (set at fixed time window of 30 seconds after the first P-wave arrival in our

290 application) for each seismogram, the final PGV measured as the maximum of the North-South and  
 291 East-West horizontal components, replaces the last P-wave predicted one, so that the evolutive,  
 292 “early” P-based, PGV predictions naturally converge toward the final PGV values.

#### 293 2.4.2 Peak ground motion prediction at “virtual” nodes

294 At each time step  $t$ , the prediction of PGV at the not-instrumented sites of the grid map, is  
 295 obtained using a physics-based, interpolation algorithm combining the available information from  
 296 recording stations and the regional scale predictions. Specifically, with the same approach as used  
 297 for the shake-map computation (Worden et al. [2010]), the PGV at the time  $t$  is obtained through  
 298 the following relationships:

299  
 300

$$301 \quad PGV^t(x, y) = \frac{\sum_{i=1}^N \left[ \frac{1}{\sigma_{onsite}^2} \cdot PGV_{onsite}^t \right] + \frac{1}{\sigma_{GMPE}^2} \cdot PGV_{GMPE}(x, y)}{\sum_{i=1}^N \left[ \frac{1}{\sigma_{onsite}^2} \right] + \frac{1}{\sigma_{GMPE}^2}} \quad \text{for all station } i \text{ with } r_{\Delta} > 0 \quad (7)$$

302

303 where:

304  $PGV_{onsite}$ : the PGV predicted at network stations from P-peak amplitudes through equations (5)  
 305 and (6);

306  $PGV_{GMPE}$ : the PGV predicted by a regional GMPE given the available estimates of earthquake  
 307 location and magnitude. In our applications we used the GMPEs derived by Bindi et al.[2011] for  
 308 Italy.

$$309 \quad \sigma_{onsite}^i = \sigma_{PGV} \cdot (1 - \exp(-\sqrt{0.6 \cdot r_{\Delta}})) \quad \text{for } r_{\Delta} \leq R_{roi}$$

$$310 \quad \sigma_{onsite}^i = \left( \sigma_{onsite}^i |_{r_{\Delta} = R_{roi}} \right) \cdot \frac{r_{max} - R_{roi}}{r_{max} - r_{\Delta}} \quad \text{for } r_{max} \geq r_{\Delta} > R_{roi} \quad (8)$$

$$311 \quad \sigma_{onsite}^i = \infty \quad r_{\Delta} \geq r_{max}$$

312 with:

- 313 -  $PGV^t(x, y)$ , the PGV predicted at the virtual node located at  $(x, y)$ ;
- 314 -  $r_{\Delta}$ , the distance between the  $i$ -th network node and the virtual node;
- 315 -  $\sigma_{GMPE}$ , the standard error of the used GMPE;
- 316 -  $\sigma_{PGV}$ , the standard error of the P-wave predicted PGV retrieved from equation 6;
- 317 -  $R_{roi}$  (roi=region of influence), the distance of the area around the network stations where the
- 318 observed data influence the PGV interpolation more than the PGV estimate through the GMPE
- 319 ( $PGV_{GMPE}$ );
- 320 -  $r_{max}$ , the limiting distance of the area where the observed data influence the interpolation.

321

322 Like their implementation in the <sup>®</sup>Shakemap algorithm (Wald et al., 2006), the parameters  $R_{roi}$

323 and  $r_{max}$  are user configurable, depending on the network aperture and inter-station distance. The

324 errors in earthquake location and magnitude on PGV predictions, which are variable and sharply

325 decreasing with time, are not explicitly considered in the present formulation but generally

326 accounted by the standard errors on GMPE and on the PGV vs P-amplitude relations. Previous tests

327 of location and magnitude determination (see Zollo et al., 2021b) using earthquakes with different

328 magnitudes and locations show that in cases of relatively high dense networks around the

329 epicenter, the errors on magnitude and location using real-time methods after only few seconds

330 become comparable to ones obtained offline and using all the network stations and the effect on

331 the predicted PGV (by GMPE) is similar to what is expected in the shakemap computation. After

332 several trials, in our application to the central Italy network we used a value of  $R_{roi} = 15 \text{ km}$  and

333  $r_{max} = 30 \text{ km}$ . The interpolation formula of equation (7) is valid for all points  $(x,y)$  at the surface,

334 except for those where stations are located, where the predicted PGV is obtained from equation 5.

335 Starting from the first P-wave arrival time, equations (7) and (8) allow predicting the PGV and its

336 uncertainty at any point of the area surrounding the epicenter. This PGV value is expected to vary

337 with time as new data become available from stations located at increasing distances from the

338 epicenter and to finally stabilize at a constant value for a high number of station amplitude data  
339 and wide P-wave time windows. We note that the maximum P-window length is chosen according  
340 to the expected S-arrival time, which is the same criterion used to determine the empirical  
341 relations (4).

342 The final output is the predicted PGV vs. time at any position (x,y) around the earthquake source,  
343 which can be finally converted to instrumental intensity through regional empirical relations (e.g.  
344 *Faenza and Michelini* [2010], for Italy) to be included in the early warning alert broadcast message.

345

### 346 **3. Application to the Mw 6.5, October 30, 2016 Norcia (Central Italy) earthquake**

347 We performed an off-line application, by simulating the real-time data streaming of the 2016  
348 October, 30, Mw 6.5 Norcia (Central Italy) earthquake (Figure 2). The event was caused by the  
349 activation of an about 20 km long system of two normal faults along the Central Apennine chain,  
350 rupturing two main slip patches (peak-slip  $\sim 3$  m) and producing a strong ground shaking and  
351 severe building damage and collapses in a wide area extending over 50 km distance around the  
352 epicenter (*Scognamiglio et al.* [2018]). According to *Scognamiglio et al.* [2018] the rupture  
353 nucleated at about 9 km depth and propagated up-dip and south-eastward along the N155°E fault  
354 with a rupture velocity of 2.8 km/sec and then triggered a secondary rupture on a smaller fault, 10  
355 km southern of the main fault epicenter, with a clockwise rotated strike direction (N210°E). The  
356 two rupture episodes produced average fault slips of 0.4 and 0.6 meters with seismic moments  
357  $5.9 \times 10^{18} Nm$  and  $2.9 \times 10^{18} Nm$ , respectively. The maps of strong ground shaking (expressed in  
358 MCS intensity scale, Peak Ground Velocity and Peak Ground Acceleration) are reported in the  
359 November 2016 INGV Working Group' report (*Gruppo di Lavoro INGV*, [2016]). The maps are  
360 computed using the peak ground shaking data available from the European Strong Motion  
361 database (*Luzi et al.* [2016]) containing the earthquake waveforms from a total set of 240 stations  
362 with a maximum epicentral distance of 673 km. The shaking intensity reported in the map ranges

363 from IV to IX, with the level of VI, corresponding to “strong perceived shaking” in the MCS scale  
364 (PGA of 4.8 %g and PGV 2.4 cm/sec), affecting a wide portion of the Central-Italy territory and  
365 extending over an area of about 100 km radius out of the epicenter.

366 For our simulation, we used the three component earthquake records acquired by 60 stations of  
367 the Italian Accelerometric Network (RAN) located within an area of 50 km radius centered at the  
368 event epicenter (Figure 2). The selected sub-network provides a rather dense azimuthal and dis-  
369 tance coverage of the source with an average inter-station spacing of 15-20 km.

370 The coefficients of eq. 1 have been preliminarily determined by a linear regression analysis using  
371 an existing earthquake data set spanning a wide magnitude ( $M_w$  3.5 – 6.5) and distance ranges ( $R$   
372 0-100 km). The dataset for calibrating the coefficients of eq.1 did not include the waveforms of the  
373 analysed  $M$  6.5 earthquake in the Norcia region. We used a total number of 286 earthquakes and  
374 3786 records (3 components each) from 504 RAN and INGV stations. The data have been gathered  
375 from the ITACA database - <http://itaca.mi.ingv.it> (Luzi et al. [2019]). Details about the calibration  
376 dataset are reported in Text S1 of the Supplemental Material. The empirical regression coefficients  
377 (A, B, C) and their uncertainties are reported in Table S1 of the Supplemental Material, together  
378 with the standard error of the regression. Plots of calibration data and scaling relationships are  
379 shown in Figure S2 of the Supplemental Material.

380 Figure 3 shows the time changes of the location error (distance in km from the INGV bulletin solu-  
381 tion) and moment magnitude, using the P-wave arrival times and peak amplitudes available at  
382 each time step, as the P-wave front progressively expands across the network. In the EEW method  
383 these data are used to update the PGV predictions at virtual nodes (eq.7) using the specific GMPE  
384 for Central Italy. The moment magnitude estimated by the EEW method is generally smaller (first  
385 estimate,  $M_w$  5.6, late estimate  $M_w$  6.2) relative to offline measures using regional and teleseismic  
386 S and surface waves (6.5+) while it is better consistent with  $M_{wp}$  (6.3) but still underestimated. In  
387 this case, the difference of -0.1 between the EEW- $M_w$  and  $M_{wp}$  can be attributed to the shallower

388 hypocentral depth (about 6 km, relative to the bulletin depth of 9 km) determined in RT by the  
389 EEW method using only near-source P-wave arrival-times. We note that despite the underestima-  
390 tion of the final earthquake depth and moment magnitude, as discussed later in this article, the  
391 EEW method can predict and track with great accuracy the peak ground shaking area, this infor-  
392 mation being used for early warning.

393 Figure 4 shows the space-time evolution of the P-wave-based prediction of instrumental intensity  
394 ( $I_{MM}$ ) (derived from PGV through the empirical relations of *Faenza and Michelini* [2010]).  
395 Snapshots are shown at different times from the event origin time.

396 The Potential Damage Zone (PDZ) is here defined as the area where the predicted peak ground  
397 velocity is larger than a threshold. In our method this is quantified in terms of instrumental  
398 intensity ( $I_{MM}$ ) (derived from PGV through the empirical relations of *Faenza and Michelini* [2010])  
399 with a threshold ( $I_{MM}=VII$ ) that, in the <sup>®</sup>shakemap implementation in Italy by INGV, is associated  
400 with the potential impact level of “very strong shaking” and “moderate” damage. The chosen PGV  
401 threshold corresponds to the minimum intensity for which damage of buildings can potentially  
402 occur in Italy, according to the reference Intensity vs PGV relationship of *Faenza and Michelini*  
403 (2010). A different intensity scale or ground motion intensity measure can be adopted and easily  
404 implemented in the approach when exporting the methodology to other areas than Italy.

405

406 The PDZ is observed to clearly expand with time, changing its shape and extent, as new data from  
407 the P waves propagating across the array are available. At its initial stage (4-5 sec, Figure 4a,b) the  
408 PDZ assumes a near-circular shape, since it is totally controlled by the GMPE-predicted PGV, with  
409 the contribution of only few near-source stations. At larger times (10-30 sec, Figure 4c,d,e) the PDZ  
410 depicts a nearly elliptical area with a predominant elongation to south-east of the epicenter. The  
411 anisotropic shape of the PDZ is the effect of larger P-wave and PGV-predicted amplitudes toward  
412 the South-East direction which is consistent with a dominant SE earthquake rupture propagation,

413 as revealed by the kinematic source modelling of near-source strong motion and GPS records  
414 (*Cheloni et al. [2017]*).

415 A precautionary first alert could be issued to the whole region of interest at the time of the first  
416 alert (around 4 sec) when a ground shaking of  $I_{MM} \geq VII$  is predicted to affect a wide near-circular  
417 area (radius 30 km) around the epicenter.

418 After about 15-20 seconds from the first P-arrival at the network, the shape of the PDZ remains  
419 stable and unchanged even adding the contribution of more distant stations (Figure 3d,e). A  
420 qualitative comparison of the 15 sec “early” shake-map (Figure 3d) with the final released by INGV  
421 (Figure 4f) shows a very good matching of  $I_{MM} > VII$  areas between P-wave predicted and final  
422 ground shaking maps. In particular, the rupture directivity toward SE is evident from the shape of  
423 the PDZ dominantly elongated in this direction.

424 We define the “time of the first alert” ( $T_{FA}$ ) as the time measured from the origin time (OT), at  
425 which the first PGV (IMM) prediction overcomes the threshold for the alert, that has been set to  
426 PGV=3.9-4 cm/sec for IMM=VII, following the scale proposed by *Faenza and Michelini [2010]*. In  
427 our simulated scenario,  $T_{FA}$ =3.6 sec, which accounts for the P-wave propagation from the  
428 earthquake depth to the surface and for the time required to get to the plateau level of LPDT  
429 curves at the two stations nearest to the epicenter.

430 The early warning system performance for this single earthquake scenario can be assessed as the  
431 ability of the system to forecast the earthquake shaking and potential impact (IMM, instrumental  
432 intensity above the threshold) in terms of the number of successful (positive and negative), missed  
433 and false alerts.

434 In detail, we can define the following criteria:

435 **Successful Alert (SA):** 
$$I_{MM}^{pred} \geq I_{MM}^{thre} \ \& \ I_{MM}^{obs} \geq I_{MM}^{thre} \quad (9a)$$

436 **Successful No-Alert (SNA):** 
$$I_{MM}^{pred} < I_{MM}^{thre} \ \& \ I_{MM}^{obs} < I_{MM}^{thre} \quad (9b)$$

437 **Missed Alert (MA):** 
$$I_{MM}^{pred} < I_{MM}^{thre} \ \& \ I_{MM}^{obs} \geq I_{MM}^{thre} \quad (9c)$$

438 **False Alert (FA):** 
$$I_{MM}^{pred} \geq I_{MM}^{thre} \text{ \& } I_{MM}^{obs} < I_{MM}^{thre} \quad (9d)$$

439 where  $I_{MM}^{thre} = VII$

440 We evaluate the performance of the EEW method at times  $T_{FA}=3.65\text{sec}$ ,  $T_{FA} + 0.5 \text{ sec}$  (4.15 sec)  
441 and  $T_{FA} + 1.5 \text{ sec}$  (5.15 sec), all times evaluated since OT (Figure 5). Indeed, we expect that the  
442 performance of the system should improve as a function of the time, since additional recorded P-  
443 amplitudes become available and more accurate estimations of the earthquake location and  
444 magnitude are derived from distant stations.

445 Figures 5a,b and c show the performance of the system at the three different times in terms of SA  
446 (dark green), SNA (light green), MA (red) and FA (yellow) with colored circles at the station  
447 locations.

448 At 3.65 sec after OT (Figure 5a), the percentage of successful alerts (SA+SNA: 57%) is slightly higher  
449 than missed/false alerts (MA+FA: 43%) considering the whole area covered by the seismic  
450 network, while it reaches near 71% when considering epicentral distances smaller than 40 km.  
451 Indeed, at this time, the majority of missed alerts are issued at the largest distances from the  
452 epicenter ( $R > 30\text{-}40 \text{ km}$ ).

453 Half a second later (Figure 5b), the shaking forecast performance highly improves, with an overall  
454 increase of the percentage of successful alerts (both SA and SNA), reaching 92%, when considering  
455 the whole 55 km radius area. At this time, a single SNA and MA are recorded, with 4 FA (6.6%).  
456 Within a circle of 40 km epicentral radius we measure 98% of SA with just one FA at a station not  
457 far from the circle. At  $T_{FA}+1.5\text{sec}$  the system performance evolves to a condition where only SA  
458 (92%) and FA (8%) are recorded. All FAs except one are recorded at outside the 40 km radius,  
459 where all sites still record all SAs except a single FAs.

460 The change with time of the relative proportion of SA, SNA,FA and MA is a typical effect of our  
461 evolutive early warning systems that will be discussed later in the paragraph "Discussion".

462 Concerning the lead-times, these are estimated as  $T_{LT} = T_S - T_{FA}$ , where  $T_S$  is the predicted S-

463 wave arrival time given the earthquake location and the average crustal velocity values ( $V_p=5.5$   
464 km/s;  $V_s=3$  km/sec) for the area. Although a more complex calculation of the lead-time using the  
465 observed S-wave arrival time could have been implemented, here we meant to provide an  
466 approximate estimate of the lead-time as a function of the distance, having preliminary verified  
467 that the observed S-wave arrival is within  $\pm 0.3$  seconds than what predicted by a homogeneous  
468 crustal velocity model.

469 The map of lead-times (Figure 6) shows values ranging from 2 s to 14.6 sec at 15 km and 55 km  
470 from the epicenter, respectively. For the considered event and station distribution the *blind-zone*,  
471 e.g., the area where the first S-waves are expected to arrive before the alert is issued, covers a  
472 circular surface with a radius of 6.5 km centered at the epicentral position.

473

#### 474 **Discussion**

475 We propose a new earthquake early warning method where the alert is issued based on the  
476 progressive tracking of the potential damage zone (depending on the chosen PGV/IMM threshold)  
477 which is mapped using a predicted PGV value resulting from the physics-based interpolation of the  
478 recorded P-amplitude and GMPE-derived PGV values. The GMPE values are determined using the  
479 earthquake location and magnitude estimated by near source recording of early P-wave signals. An  
480 update of PGV/IMM predictions is done as new locations and P-wave data are available from more  
481 distant stations. Since it is based on the recorded ground motion P-amplitudes at stations around  
482 the epicenter, the proposed technique naturally accounts for the spatial variability of strong  
483 ground motion related source (i.e., rupture directivity), crustal wave propagation and site  
484 amplification as inferred from the early P-signals.

485 The onsite PGV at instrumented sites is predicted from the P-peak acceleration, velocity and  
486 displacement values measured on the original vertical component record. In this study, the  
487 empirical relations  $\log \text{PGV vs } \log (P_d, P_v, P_a)$  have been determined and calibrated for the Central

488 Italy region using the available waveform data-bank for previous earthquakes in the magnitude  
489 range 3-6.5 and distance interval 10-100 km.

490 The use of the three P-amplitude, observed parameters showed to improve, in general, the  
491 accuracy of the predicted PGV relative to the use of a single parameter, since they carry on  
492 information about the P-amplitude in different frequency bands. In addition, since the P-peak  
493 amplitude for moderate-large earthquakes is expected to increase with time from the first P-  
494 arrival, the method implements an algorithm allowing to start measuring the P-amplitude only  
495 after the LPDT curves reach their plateau. This would make more robust the technique by reducing  
496 the number of missed alerts at the expenses of a longer P-wave time window to explore. Recently  
497 *Colombelli et al.* [2014, 2020] showed that the initial slope of the LPDT curves scales inversely with  
498 the earthquake magnitude, suggesting that this initial slope parameter could be used as a proxy for  
499 the rapid assessment of the earthquake size during an ongoing rupture. Future developments of  
500 the described method will include initial slope measurements to provide constraints on the  
501 ongoing event magnitude, to be used for a faster time of the first alert.

502 The proposed methodology integrates the principles of onsite EEW methods with those used for  
503 network-based approaches, to provide reliable and physics-based estimations of the expected  
504 shaking distribution. An intrinsic advantage of the methodology is the capacity of being adapted to  
505 a variety of potential stakeholders and target applications, that could make use of outcomes of the  
506 method in different ways. For example, on-site estimates could be used to control dedicated  
507 actions at specific sites (such as industrial settlements, schools, hospitals), while distributed targets  
508 (as the case of railway applications) could benefit from the real-time regional mapping of the  
509 expected shaking to trigger automatic emergency measures as slowing-down/arrest high-speed  
510 trains, disrupting the gas/electric energy supply to a pipeline, halting the high-way circulation of  
511 vehicles transporting hazardous materials.

512 The off-line application of the EEW method to the M 6.5 October,30, 2016 Norcia earthquake in

513 Central Italy shows the reliability and robustness of the methodology. It provides a rapid alert  
514 message with a time-varying assessment of the earthquake shaking and potential impact as  
515 obtained by the algorithm of data interpolation able to build a realistic, P-wave-based, “early”  
516 shake map. We showed that the latter is very consistent with the shake-map computed by INGV  
517 tens of minutes after the earthquake occurrence, using the recorded PGV data on the horizontal  
518 components at strong motion stations over a wide distance range.

519 The considered scenario case confirms a good performance of the system in terms of reliability of  
520 the predicted intensity map which naturally includes the spatially variable ground motion shaking  
521 as originated by source directivity effects, although inferred from near-source recorded P-  
522 amplitudes. This is already visible on maps after few seconds from the first P-wave recorded at the  
523 near-epicenter stations.

524 The rapidity of the system in processing data and releasing the warning along with the reliability of  
525 ground shaking predictions may depend on the network density and azimuthal coverage in the  
526 epicentral area. However, the joint use of regional-scale and on-site predictions for the ground  
527 shaking distribution is expected to provide better constrained predictions, even in those situations  
528 where the distribution and coverage of stations are non-optimal. This could be the case, for  
529 example, of off-shore subduction earthquakes (such as the 2011, Tohoku-Oki earthquake), for  
530 which we expect that the addition of coastal stations will strongly constrain the regional-predicted  
531 shaking distribution, as discussed by Colombelli et al., (2012) when rapidly mapping the Potential  
532 Damage Zone for this event.

533 We showed that the capability of the EEW system to predict the strong motion above the  
534 threshold improves with time. Only 1.5 sec after the TFA (5.15 sec after the OT) the performance  
535 of the system in predicting the event peak shaking is very high: in the area of 40 km radius around  
536 the epicenter, that impacted an Intensity MCS VIII-IX as estimated by INGV shakemap), all 42  
537 instrumented sites except one showed a successful alert with only one false alarm. Considering the

538 calculated blind-zone of 6.5 km radius, there is still a wide annular area, where the alert could have  
539 reached the population before the strong ground shaking occurrence.

540 In Figure 5c, the circular blind-zone and lead-times are calculated at  $T_{FA}=3.65$  sec which  
541 corresponds to the time of the P-waves detected at the first two stations, and when the first  
542 location, magnitude estimations and peak amplitudes are available. According to this simulation,  
543 only 1 municipality of the 170 located within 55 km of the epicenter and belonging to the regions  
544 of Abruzzo, Marche, Umbria and Lazio, would be located within the blind-zone. For these 2  
545 municipalities the minimum negative lead-time is -0.5 sec at the town of Norcia, i.e. half-second is  
546 the maximum time in advance of the S-wave arriving at these sites before the alert issuing.

547 Even considering a later first alert, i.e., at 5.15 sec after the OT, the calculated blind-zone radius  
548 would have been 15 km long. 165 municipalities, located in the 15-55 km circular ring around the  
549 epicenter show positive lead-times, and might have been alerted 2 to 14.5 sec in advance to the  
550 arrival of the first S-wave at those sites.

551 At  $T_{FA}=3.65$  sec, for 26 of the 60 accelerometric station sites, located at epicentral distances  
552 between 25 and 55 km, the EEW system incorrectly predicts a PGV below the threshold (e.g. a  
553 missed alert, MA). The numbers of MA at  $T_{FA}=3.65$  sec for distant sites is mainly due to the  
554 underestimated PGV predicted by the GMPE with an initial lower magnitude as evaluated from  
555 near-source stations while using short P-wave time windows. As the time increases, larger portions  
556 of the P-wave time window are considered for the analysis and sites previously labelled as MA or  
557 SNA evolve towards SA and FA, respectively, with a final picture where only successful and false  
558 alerts are declared at the network. This is a common characteristic of similar time-evolutive EEW  
559 system that naturally tend with time to increase SA and FA at the expenses of MA and SNA.

560 This effect can be explained starting from the definitions of SA, SNA, MA and FA, provided by  
561 equations 9a,d. For each of the four possible situations, indeed, the second member of inequalities  
562 (related to  $I_{MM}^{obs}$ ) does not change with time at the recording nodes. The first condition (related to

563 the predicted intensity ( $I_{MM}^{pred}$ ), instead, may evolve with time. Specifically, the instrumental  
564 intensity is continuously predicted from the vertical  $P_x$  amplitude and, by definition of the  $P_x$   
565 parameter, it can only increase or remain stable with time, so that once the predicted intensity has  
566 exceeded the threshold for warning declaration, the alert cannot be cancelled. With this in mind,  
567 the prediction performance at any recording sites may potentially evolve with time from SNA (light  
568 green) to FA (yellow) or from MA (red) to SA (dark green). Other transitions between alert states  
569 are, de facto, not possible.

570 Indeed, initial PGV underestimations leading to MA and SNA can be related to P-window lengths  
571 shorter than the half-duration of the earthquake source time function (*Colombelli and Zollo*  
572 [2015]) resulting in an initial magnitude underestimation. As the P-window time increases, since  
573 the max P-peak amplitude can only increase, the MAs can be confirmed or evolve in Successful  
574 Alerts, if the predicted PGV becomes larger than the threshold.

575 On the other hand, SNAs can be confirmed or, if the predicted PGV increases, can only evolve in  
576 False Alerts. With similar arguments, we note that, since the predicted PGV can only increase with  
577 an enlarged P-window, both all SAs and FAs would not change their status.

578 Building an EEW system that evolves with time in a manner that missed alerts and successful no-  
579 alerts tend to be minimized while increasing the number of successful alerts represent a strong  
580 advantage of the proposed EEW method, although this result is achieved at the expenses of an  
581 increase of false alerts. A similar conclusion was drawn by *Minson et al.* [2021] who analyzed the  
582 ideal case of a rail system in California's San Francisco Bay Area to explore potential uses of a  
583 network-based EEW system for rail systems.

584 With this regard, we note that, at the first alert time and after, the relative percentage of SA, SNA,  
585 FA and MA critically depends on the predicted PGV (through the measured  $P_x$  (eq.4)) and on the  
586 chosen IMM (or PGV) threshold, due to the natural distribution and scattering of data around the  
587 empirical laws that are used to predict PGV from the P-peak amplitude. This is clearly depicted in

588 Figure 6, that shows an example of the used empirical attenuation relations between PGV and P<sub>v</sub>.  
589 For a given PGV threshold and a measured value of P<sub>v</sub>, the diagram Predicted PGV vs measured P-  
590 amplitude is partitioned in 4 regions, around the predicted PGV point: the regions of SAs (dark-  
591 green, top-right), SNAs (light-green, bottom-left), FA (yellow, bottom-right) and MA (red, top-left).  
592 It is clear how the relative proportion of SA, SNA, FA and MA depends on the measured P<sub>x</sub> and  
593 selected PGV threshold, that can change with time as the P<sub>x</sub> value and associated predicted PGV  
594 increase. This example demonstrates that if PGV's predictions are based on empirical regressions  
595 of P-wave amplitude data, the optimal future solution to improve the performance of the time-  
596 evolutive EEW system is to refine and make more robust the empirical PGV prediction laws. This  
597 will be possibly achieved using AI-based machine learning approaches or through the exploration  
598 of more complex multi-parametric regression models (which includes site, azimuthal, distance  
599 effects) than the ones represented by eqs. 4.

## 600 **Conclusions**

601 We have proposed an EEW method which uses the real-time P-peak amplitudes progressively  
602 measured at a dense accelerometric network around the epicenter to track the time-evolving  
603 potential damage zone, i.e the area within which the strong ground motion is expected to exceed a  
604 given instrumental intensity threshold. Compared with source-based early warning approaches,  
605 where the event magnitude and location are used to issue an alert, our method follows a shaking-  
606 forecast-based strategy, where the alert is rather issued upon the prediction of the strong ground  
607 shaking amplitudes at sites to be secured during the earthquake emergency. The method is time-  
608 evolutive, since the shape of the potential damage zone is modeled according to new data  
609 incoming from progressively distant stations and larger P-wave windows are assimilated by the  
610 EEW system. The potential damage zone is traced by combining the Peak Ground Velocity values  
611 predicted by early P-wave amplitudes at accelerometer sites with values predicted by the regional  
612 GMPE using the updated values of location and moment magnitude.

613 We showed that the P-wave-based, early shake-map well reproduce the elongation and shape of  
614 the final shake-map and the extent of the area driven by the rupture directivity and that suffered  
615 the largest shaking and damage during the October 30, 2016, M 6.5 Central Italy event.

616 The offline simulation of the EEW method illustrates a common characteristic of time-evolutive  
617 systems, i.e. while trying to reduce uncertainties as much as possible, it will not be possible to  
618 eliminate the occurrence of false and missed alarms, so it is necessary for the end-user to accept  
619 these eventualities and account for them in a probabilistic frame to be implemented in a user-  
620 specific, decision-making strategy for minimizing the earthquake impact in real-time.

621 Despite these intrinsic limitations, a time-evolutive EEW as the one illustrated in our study, can  
622 help to implement strategies to mitigate the earthquake impact on false alert-tolerant users, who  
623 set the threshold and time of the alerts based on their specific risk mitigation actions, thus  
624 averaging between the requirement of the system to be fast in alerting (long lead-times) and  
625 accurate in the shaking predictions (reduced number of missed and false alarms).

## 626 **Acknowledgements**

627 The authors thank the members of the Early Warning Group at the Seismological Laboratory  
628 (RISSCLAB) of the Department of Physics of the University of Naples Federico II, for their support  
629 and contribution of ideas during the research development. The research has been partially  
630 funded by :

631 - the Italian Ministry of University and Research (MUR) through the National Operative Pro-  
632 gramme (PON-AIM 218 AIM1834927 – 3) and the project European Plate Observing System  
633 (EPOS)-Italia

634 - the Department of Civil Protection (DPC), through a research contract with the University of  
635 Naples Federico II

## 636 **Conflict of interest**

637 The authors declare no conflicts of interest relevant to this study

638 **Data Availability Statement**

639 All of the data used to undertake this research are freely available. The specific source for the data  
640 is provided in the text and summarized below.

641 - Strong-motion records of the Mw 6.5, October 30, 2016 Norcia (Central Italy) earthquake  
642 acquired by the Italian Accelerometric Network (RAN) owned by the Department of Civil  
643 Protection – ITACA V3.2 Waveform DataBase available at <https://itaca.mi.ingv.it/>

644

645 **References**

646 Alcik, H., Ozel, O., Apaydin, N., Erdik, M., 2009. A study on warning algorithms for Istanbul  
647 earthquake early warning system. *Geophys. Res. Lett.* 36, L00B05.

648 <https://doi.org/10.1029/2008GL036659>

649 Allen, R.M., Melgar, D., 2019. Earthquake Early Warning: Advances, Scientific Challenges, and  
650 Societal Needs. *Annu. Rev. Earth Planet. Sci.* 47, 361–388. [https://doi.org/10.1146/annurev-earth-](https://doi.org/10.1146/annurev-earth-053018-060457)  
651 [053018-060457](https://doi.org/10.1146/annurev-earth-053018-060457)

652 Allen, R. M., and A. Ziv (2011), Application of real-time GPS to earthquake early warning, *Geophys.*  
653 *Res. Lett.*, 38, L16310, doi:10.1029/2011GL047947

654 Allen RM, Gasparini P, Kamigaichi O, Böse M. 2009. The status of earthquake early warning around  
655 the world: an introductory overview. *Seismol. Res. Lett.* 80(5):682–93

656

657 Bindi, D., Pacor, F., Luzi, L., Puglia, R., Massa, M., Ameri, G. and R. Paolucci (2011) Ground motion  
658 prediction equations derived from the Italian strong motion database. *Bull Earthquake Eng* (2011)  
659 9:1899–1920, DOI 10.1007/s10518-011-9313-z

660 Boore, David & Stephens, Chris & Joyner, William. (2002). Comments on baseline correction of  
661 digital strong-motion data: examples from the 1999 Hector Mine, California, earthquake. *Bulletin*

662 of the Seismological Society of America. 92. 1543-1560.

663 Böse, M., Thomas H. Heaton, Egill Hauksson (2012) Real-time Finite Fault Rupture Detector  
664 (FinDer) for large earthquakes, *Geophysical Journal International*, Volume 191, Issue 2, November,  
665 Pages 803–812, <https://doi.org/10.1111/j.1365-246X.2012.05657.x>

666 Caruso, A., S. Colombelli, L. Elia, M. Picozzi and A. Zollo, (2017) An onsite alert level early warning  
667 system for Italy, *J. Geophys. Res. Solid Earth*, 122, doi 10.1002/2016JB01340

668 Cheloni, D., et al. (2017), Geodetic model of the 2016 Central Italy earthquake sequence inferred from InSAR and  
669 GPS data, *Geophys. Res. Lett.*, 44, 6778–6787, doi:10.1002/2017GL073580

670 Colombelli, S., Zollo, A., Festa, G., and Kanamori, H. (2012), Early magnitude and potential damage  
671 zone estimates for the great Mw 9 Tohoku-Oki earthquake, *Geophys. Res. Lett.*, 39, L22306,  
672 doi:[10.1029/2012GL053923](https://doi.org/10.1029/2012GL053923).

673 Colombelli, S., R. M. Allen, and A. Zollo (2013), Application of real-time GPS to earthquake early  
674 warning in subduction and strike-slip environments, *J. Geophys. Res. Solid Earth*, 118,  
675 doi:10.1002/jgrb.50242

676 Colombelli, S., A. Zollo, G. Festa, and M. Picozzi (2014), Evidence for a difference in rupture  
677 initiation between small and large earthquakes, *Nat. Commun.*, 5, 3958,  
678 doi:10.1038/ncomms4958.

679 Colombelli, S., Caruso, A., Zollo, A., Festa, G. and Kanamori, H. (2015), A P wave-based, on-site  
680 method for earthquake early warning. *Geophys. Res. Lett.*, 42: 1390– 1398. doi:  
681 10.1002/2014GL063002

682 Colombelli, S., and A. Zollo (2015) Fast determination of earthquake magnitude and fault extent  
683 from real-time P-wave recordings, *Geophysical Journal International*, Volume 202, Issue 2, , Pages  
684 1158–1163, <https://doi.org/10.1093/gji/ggv217>

685 Colombelli, Simona & Festa, Gaetano & Zollo, Aldo. (2020). Early rupture signals predict the final  
686 earthquake size. *Geophysical Journal International*. 223. 692-706. 10.1093/gji/ggaa343.

- 687 Clinton J, Zollo A, Marmureanu A, Zulfikar C, Parolai S. 2016. State-of-the art and future of  
688 earthquake early warning in the European region. *Bull. Earthq. Eng.* 14(9):2441–58
- 689 Faenza L. and A. Michelini, (2010). Regression analysis of MCS intensity and ground motion  
690 parameters in Italy and its application in ShakeMap, *Geophysical Journal International*, Volume  
691 180, Issue 3, March 2010, Pages 1138–1152, <https://doi.org/10.1111/j.1365-246X.2009.04467.x>
- 692 Gruppo di Lavoro INGV sul terremoto in centro Italia (2016). Rapporto di sintesi sul Terremoto in  
693 centro Italia Mw 6.5 del 30 ottobre 2016, doi: 10.5281/zenodo.166019 (in Italian).
- 694 Grapenthin, R., Johanson, I. A., and Allen, R. M. (2014), Operational real-time GPS-enhanced  
695 earthquake early warning, *J. Geophys. Res. Solid Earth*, 119, 7944– 7965,  
696 doi:10.1002/2014JB011400.
- 697 Kanamori H. Real-time seismology and earthquake damage mitigation. *Ann Rev Earth Planet Sci*  
698 2005;33:195–214, doi:10.1146/annurev.earth. 33.092203.122626.
- 699 Kodera, Y., Yasuyuki Yamada, Kazuyuki Hirano, Koji Tamaribuchi, Shimpei Adachi, Naoki  
700 Hayashimoto, Masahiko Morimoto, Masaki Nakamura, Mitsuyuki Hoshihara (2018) The Propagation  
701 of Local Undamped Motion (PLUM) Method: A Simple and Robust Seismic Wavefield Estimation  
702 Approach for Earthquake Early Warning. *Bulletin of the Seismological Society of America* , 108 (2):  
703 983–1003. doi: <https://doi.org/10.1785/0120170085>
- 704 Lomax, A., J. Virieux, P. Volant and C. Berge, 2000. Probabilistic earthquake location in 3D and  
705 layered models: Introduction of a Metropolis-Gibbs method and comparison with linear locations,  
706 in *Advances in Seismic Event Location* Thurber, C.H., and N. Rabinowitz (eds.), Kluwer, Amsterdam,  
707 101-134..
- 708 Lomax, A., C. Satriano and M. Vassallo (2012), Automatic picker developments and optimization:  
709 FilterPicker - a robust, broadband picker for real-time seismic monitoring and earthquake early-  
710 warning, *Seism. Res. Lett.* , 83, 531-540, doi: 10.1785/gssrl.83.3.531
- 711 Luzi L., Puglia R, Russo E & ORFEUS WG5 (2016). Engineering Strong Motion Database, version 1.0.

- 712 Istituto Nazionale di Geofisica e Vulcanologia, Observatories & Research Facilities for European  
713 Seismology. doi: 10.13127/ESM
- 714 Minson, S.E., Baltay, A.S., Cochran, E.S. et al. The Limits of Earthquake Early Warning Accuracy and  
715 Best Alerting Strategy. *Sci Rep* 9, 2478 (2019). <https://doi.org/10.1038/s41598-019-39384-y>
- 716 Nakamura Y, Tucker BE. 1988. Japan's earthquake warning system: should it be imported to  
717 California? *Calif. Geol.* 41(2):33–40
- 718 Minson, S.E., Cochran, E.S., Wu, S., Noda, S. (2021). A Framework for Evaluating Earthquake Early  
719 Warning for an Infrastructure Network: An Idealized Case Study of a Northern California Rail  
720 System. *Front. Earth Sci.* 9, 620467. <https://doi.org/10.3389/feart.2021.620467>
- 721 Nazeri, S., Colombelli, S. & Zollo, A. (2019), "Fast and accurate determination of earthquake moment, rupture  
722 length and stress release for the 2016-2017 Central Italy seismic sequence", *Geophysical Journal  
723 International*, Volume 217, Issue 2, Pages 1425–1432, doi.org/10.1093/gji/ggz097
- 724 Odaka, T., K. Ashiya, S. Tsukada, S. Sato, K. Ohtake, and D. Nozaka (2003). A new method of quickly  
725 estimating epicentral distance and magnitude from a single seismic record. *Bulletin of the  
726 Seismological Society of America* 93, 526–532.
- 727 Scognamiglio, L., Tinti, E., Casarotti, E., Pucci, S., Villani, F., Cocco, M., et al. (2018). Complex fault  
728 geometry and rupture dynamics of the MW 6.5, 30 October 2016, central Italy earthquake. *Journal  
729 of Geophysical Research: Solid Earth*, 123, 2943– 2964. <https://doi.org/10.1002/2018JB015603>
- 730 Satriano, C., Lomax, A., Zollo, A. (2008). Real-Time Evolutionary Earthquake Location for Seismic  
731 Early Warning. *Bulletin of the Seismological Society of America*, 98 (3): 1482–1494.  
732 <https://doi.org/10.1785/0120060159>
- 733 Trugman, D. T., Page, M. T., Minson, S. E., & Cochran, E. S. ( 2019). Peak ground displacement  
734 saturates exactly when expected: Implications for earthquake early warning. *Journal of  
735 Geophysical Research: Solid Earth*, 124, 4642– 4653. <https://doi.org/10.1029/2018JB017093>
- 736 Yamamoto, S., Rydelek, P., Horiuchi, S., Wu, C., and Nakamura, H. (2008), On the estimation of

737 seismic intensity in earthquake early warning systems, *Geophys. Res. Lett.*, 35, L07302,  
738 doi:[10.1029/2007GL033034](https://doi.org/10.1029/2007GL033034).

739 Wald, D. J., C. B. Worden, V. Quitoriano, and K. L. Pankow (2006). ShakeMap® Manual,  
740 Technical Manual, Users Guide, and Software Guide;  
741 <http://pubs.usgs.gov/tm/2005/12A01/pdf/508TM12-A1.pdf>.

742 Worden, C. B., Wald, D. J., Allen, T. I., Lin, K. Garcia, D. and G. Cua; A Revised Ground-Motion and  
743 Intensity Interpolation Scheme for ShakeMap (2010) *Bulletin of the Seismological Society of*  
744 *America* 100 (6): 3083–3096. doi: <https://doi.org/10.1785/0120100101>

745 Wu, Y. M., and H. Kanamori (2005), Experiment of an on-site method for the Taiwan Early Warning  
746 System, *Bull. Seismol. Soc. Am.*, 95, 347–353, doi:10.1785/0120040097

747 Wu, Y.-M., and L. Zhao (2006), Magnitude estimation using the first three seconds P-wave  
748 amplitude in earthquake early warning, *Geophys. Res. Lett.*, 33, L16312,  
749 doi:10.1029/2006GL026871

750 Zollo, A., Amoroso, O., Lancieri, M., Wu, Y. And H. Kanamori (2010). A Threshold-based  
751 Earthquake Early Warning using dense accelerometer networks. *Geophysical Journal International*.  
752 183. 10.1111/j.1365-246X.2010.04765.x.

753 Zollo, A., Lancieri, M. & Nielsen, S. (2006) Earthquake magnitude estimation from peak amplitudes  
754 of very early seismic signals on strong motion. *Geophys. Res. Lett.* 33, L23312,  
755 <https://doi.org/10.1029/2006GL027795> (2006)

756 Zollo, A., Nazeri, S. and S. Colombelli, (2021a) Earthquake Seismic Moment, Rupture Radius, and  
757 Stress Drop From P-Wave Displacement Amplitude Versus Time Curves, *IEEE Transactions on*  
758 *Geoscience and Remote Sensing*, vol. 60, pp. 1-11, 2022, Art no. 5912211, doi:  
759 10.1109/TGRS.2021.3119909.

760 Zollo, A., Caruso, A., De Landro, G., Colombelli, S., & Elia, L. (2021b). A Bayesian method for real-  
761 time earthquake location using multiparameter data. *Journal of Geophysical Research: Solid Earth*,  
762 126, e2020JB020359. <https://doi.org/10.1029/2020JB020359>

763  
764

#### 765 Figure Captions

766 **Figure 1: Block Diagram of the method.** The figure shows the block diagram of the methodology,  
767 in which on-site PGV predictions (left) are combined with network-based PGV predictions (center),  
768 for a refined, real-time shake map construction and dissemination of alerts at target sites (right).

769

770 **Figure 2: Example of seismogram and LPDT curves .** a) Examples of acceleration records at  
771 increasing distance from the source (from top to bottom). Colors are used to identify the  
772 corresponding stations in panels b) and c) and for each station, the hypocentral distance is  
773 reported on the plot. b) LPDT curves computed at each station, starting at the P-wave arrival  
774 (shown with a coloured circle on each seismogram) and steeping at the expected arrival of S-  
775 waves. For a matter of visualization, the LPDT curves are initialized to a common, amplitude value.  
776 c) Map of the epicentral position of the earthquake and recording stations within a maximum  
777 distance of 50 km.

778

779 **Figure 3: Time evolutive estimation of event location and magnitude.** The plot shows the  
780 comparison between the real-time earthquake location (top panel) with the bulletin solution, both  
781 for the epicentral position (black line) and for the earthquake depth (grey line). The bottom panel  
782 shown the real-time estimate of the earthquake magnitude, as average values (gray circles) and  
783 their uncertainties (error bars). Magnitude estimates form available agencies are also shown for  
784 reference, with horizontal lines. In both panels, the x-axis shows time in seconds form the origin

785 time of the event.

786

787 **Figure 4: Result for the 2016-10-30 Mw6.5 Norcia (Italy) earthquake.** Examples of the  
788 evolutionary, P-wave based early shake maps at different seconds from origin time (reported in  
789 each panel). In each panel, stations are the gray triangles, the red star is the epicenter of the event  
790 and the contour lines for the predicted intensity levels VII and VIII are also shown. The bottom-  
791 right panel is the reference INGV shake map.

792

793 **Figure 5: Performance Evaluation.** The figure shows the performance of the system at the three  
794 different times in terms of Successful Alerts (dark green), Successful No-Alerts (light green),  
795 Missed Alerts (red) and False Alerts (yellow) at each station position. In all panels, the yellow circle  
796 is the 40km radius around the epicenter, while the red circle represents the blind zone.

797

798 **Figure 6: Lead-Time map.** The figure shows values the map of available lead-times in the  
799 epicentral area and the position of municipalities that could have benefit from the warning. Each  
800 circle on the map represents the area in which the corresponding lead-time (indicated in white)  
801 would have been available.

802

Figure1.

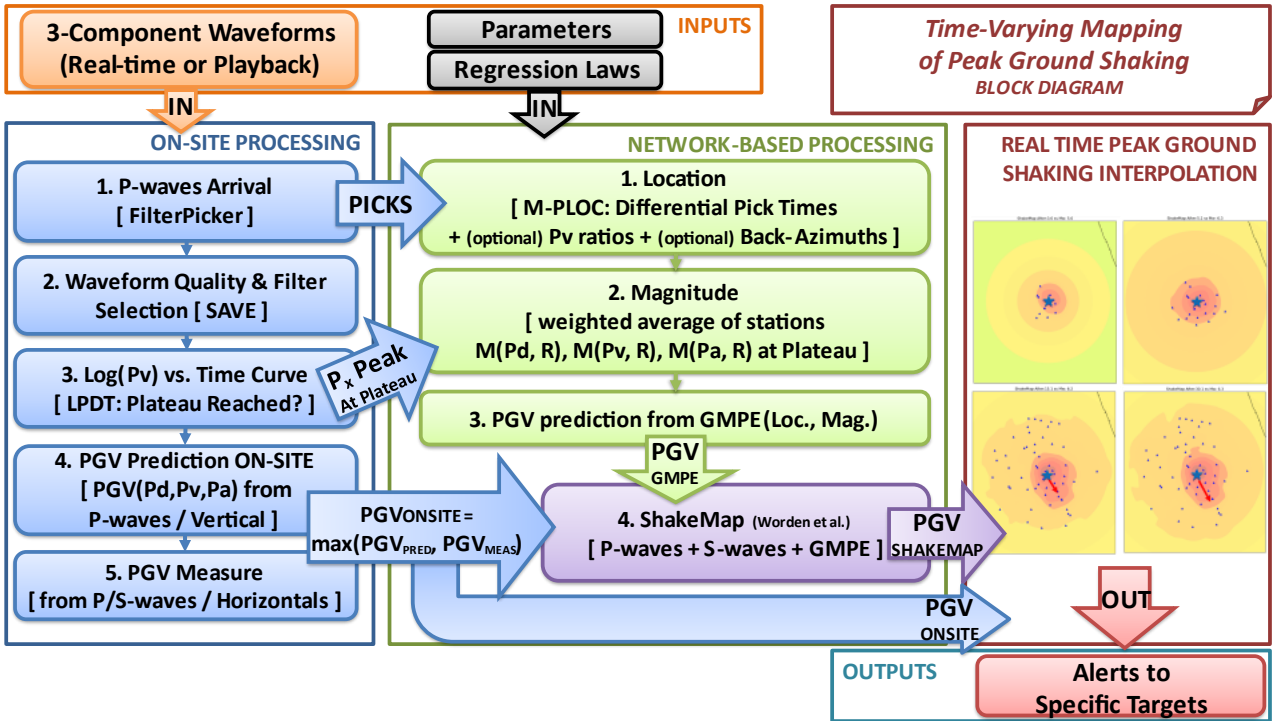


Figure2.

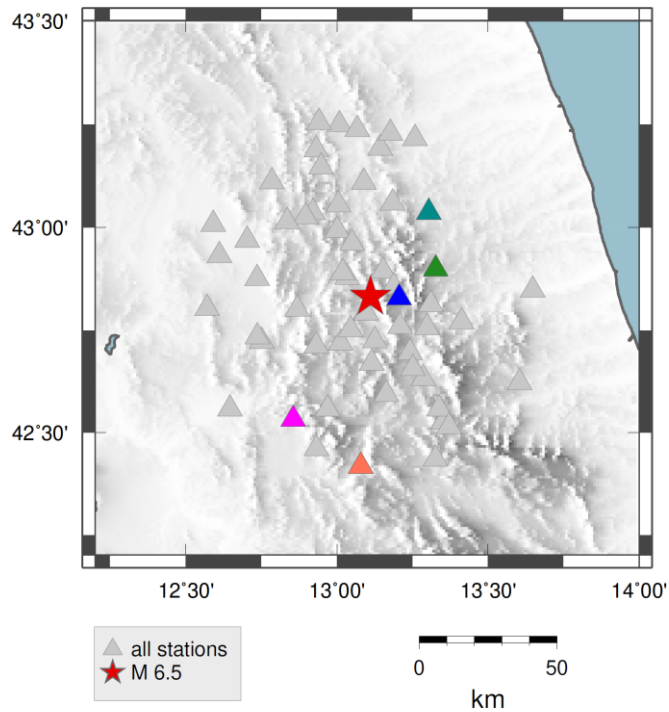
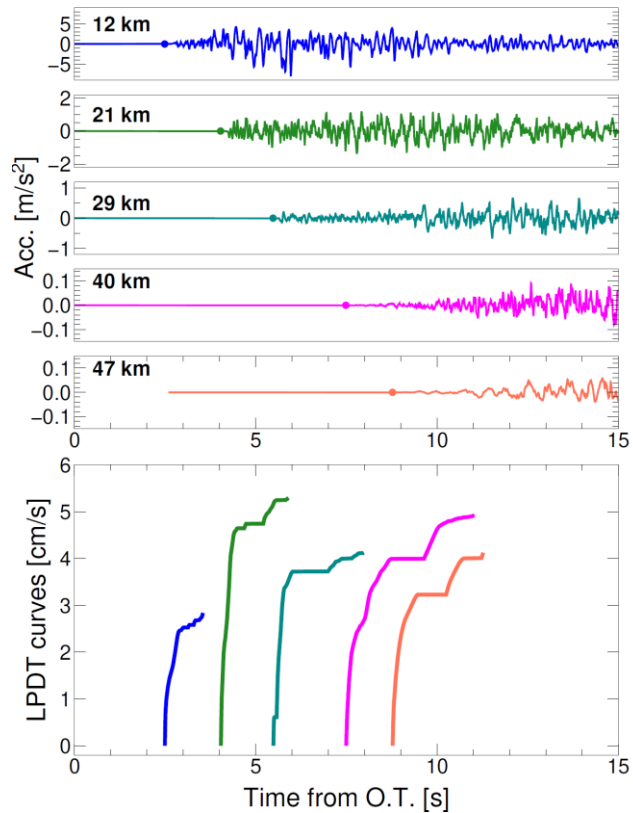


Figure3.

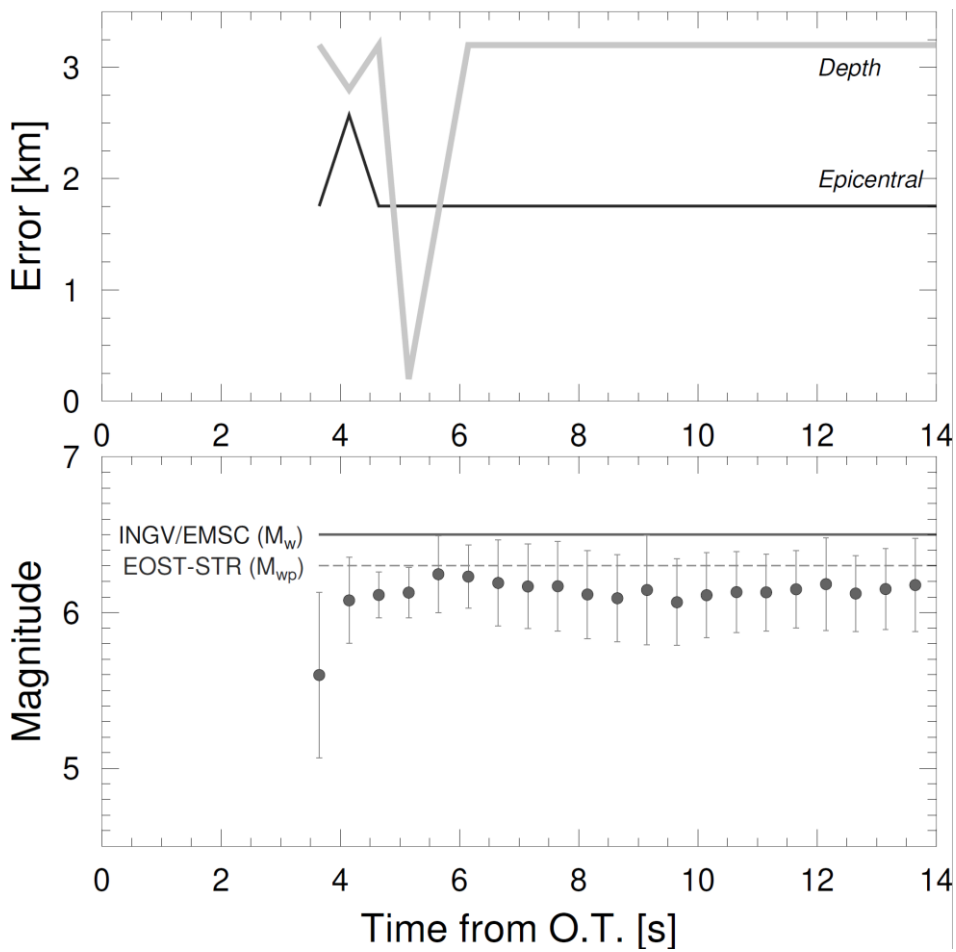
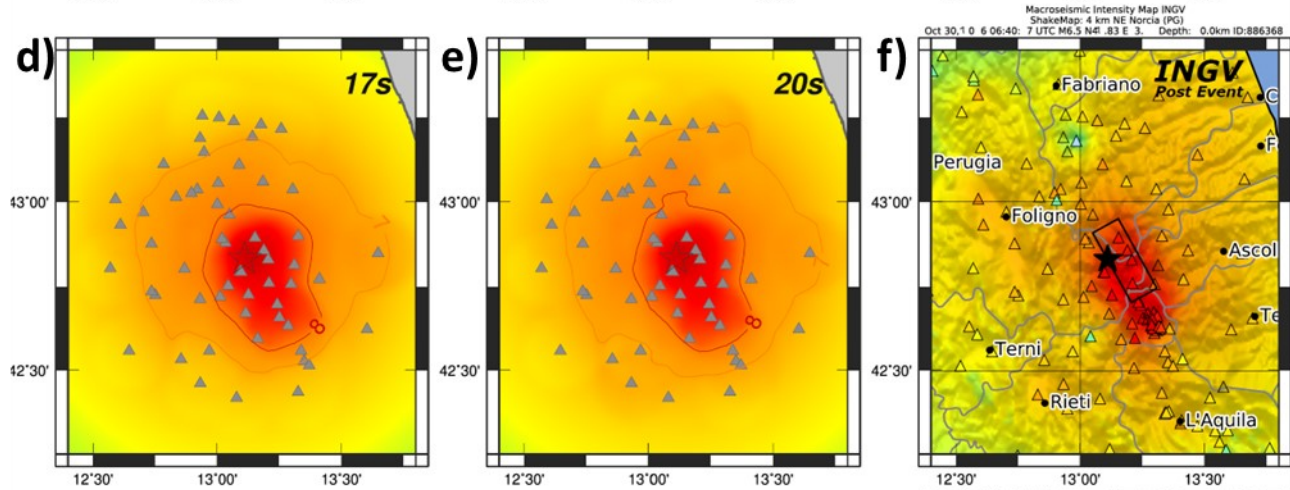
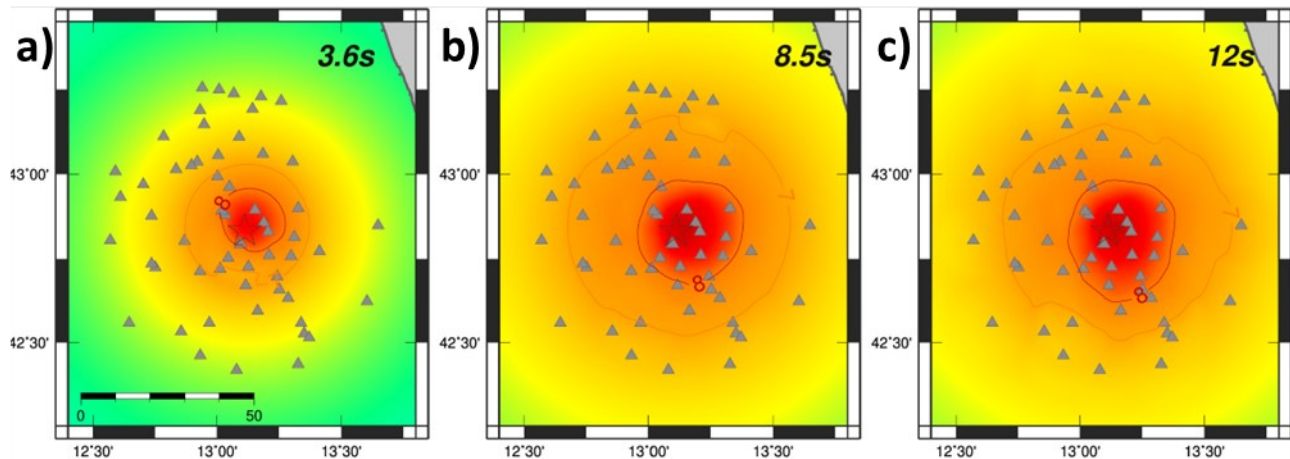


Figure4.



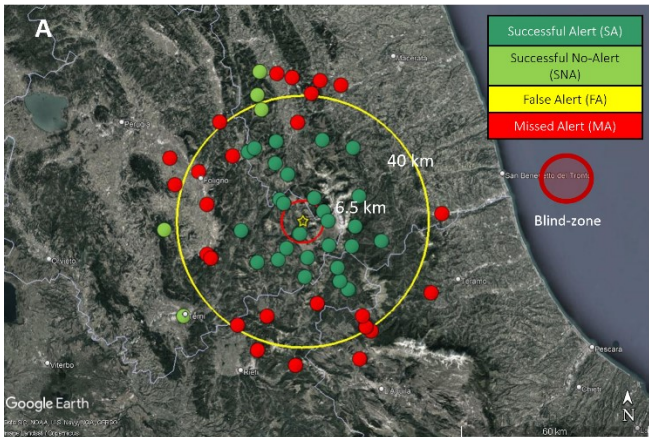
Macroseismic Intensity Map INGV  
 ShakeMap: 4 km NE Norcia (PG)  
 Oct 30.1.0 6 06:40: 7 UTC M6.5 N46.83 E 3 Depth: 0.0km ID:886568

| SHAKE:     | None | Very Weak | Weak | Light      | Moderate | Strong   | Very Strong    | Severe | Violent    | Extreme |
|------------|------|-----------|------|------------|----------|----------|----------------|--------|------------|---------|
| DAMAGE:    | None | None      | None | Very Light | Light    | Moderate | Moderate/Heavy | Heavy  | Very Heavy |         |
| PEARSON:   | 0.00 | 0.1       | 0.25 | 0.5        | 0.75     | 1.0      | 1.5            | 2.0    | 3.0        | 4.0     |
| PEWENBERG: | 0.0  | 0.1       | 0.25 | 0.5        | 0.75     | 1.0      | 1.5            | 2.0    | 3.0        | 4.0     |
| INTENSITY: | I    | II        | III  | IV         | V        | VI       | VII            | VIII   | IX         | X       |

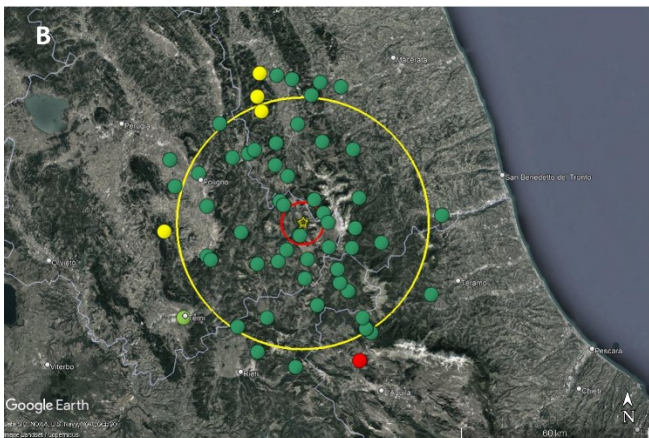
Scale based on Fattori and Rebecchi (2003) (S, L, V, VI, VII, VIII, IX, X)  
 S: Seismic Instrument = Reported Intensity \* Epicenter □: rupture

Figure5.

Time TFA=3.65 sec since OT



Time 4.15 sec since OT



Time 5.15 sec since OT

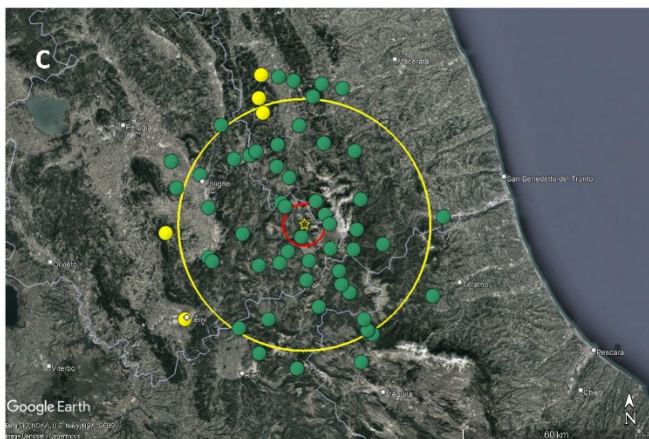


Figure6.

